Bifunctional porous Co-doped NiO nanoflowers electrocatalysts for rechargeable zinc-air batteries

Jinmei Qian[a], Xiaosong Guo[b], Tongtong Wang[a], Peitao Liu[a], Hong Zhang[a,*], Daqiang Gao[a,*]

[a] Key Laboratory for Magnetism and Magnetic Materials of MOE, Key Laboratory of Special Function Materials and Structure Design of MOE, Lanzhou University, Lanzhou, 730000, China
[b] College of Materials Science and Engineering, Qingdao University of Science and Engineering, Qingdao, Shandong, 266061, China

ABSTRACT

Zinc-air batteries (ZnABs) represent one of the most promising options to power next-generation electric vehicles owing to their high theoretical energy density and reliable safety. However, their further development and application is hampered due to the lack of high-efficiency bifunctional air electrocatalysts. Herein, porous Co-doped NiO nanoflowers (Co-NiO NFs) with outstanding electrocatalytic activity and stability toward oxygen evolution reaction (ORR) and oxygen reduction reaction (OER) is reported for the first time, including a positive half-wave potential (0.79 V) for ORR and a small overpotential (1.53 V at 10 mA cm^{-2}) for OER. Firstly, the synergistic effect between the sound two-dimensional (2D) hexagonal framework and numerous nanopores inside the nanosheets offers an available surface for O_2 adsorption/diffusion, and a large effective electrochemical active surface area for exploring and utilizing more active sites. Secondly, Co dopants can effectively increase the conductivity of pristine NiO nanoflowers (NFs) and simultaneously enhances the intrinsic ORR and OER activity. Notably, the liquid ZnABs with engineered Co-NiO NFs electrode exhibits a high discharge peak power density of 93 mW cm^{-2}, a satisfactory specific capacity of 830 mA h g^{-1} at the current density of 5 mA cm^{-2}, together with excellent cycling stability of 110 h at 2 mA cm^{-2}. Additionally, the corresponding all-solid-state ZnABs assembled with Co-NiO NFs shows a long durability with the stable charge-discharge cycles of 6 h and good flexible nature.

1. Introduction

Developing of novel, clear, high performance energy conversion and storage systems is highly critical and inevitable to address the ever increasing detrimental effects of the excessive consumption of traditional fuels on energy and environment [1–5]. As one type of metal-air batteries, Zinc-air batteries (ZnABs) have received revived interest recently for further large-scale energy applications because of a high theoretical energy density of 1086 Wh kg^{-1} (about five times than the current lithium-ion technology), better safety and lower cost [6–8]. In addition, ZnABs can offer the highest available energy density of any primary battery systems due to oxygen can be directly got from the ambient air, and they are considered as the best option to replace lithium-air batteries for further electric vehicles applications [9–11]. However, their performances and widespread application are impeded by their limitations in power density and energy efficiency due to the inefficiency of air catalysts available. Additionally, extending cycle life of rechargeable ZnABs is urgent due to the lack of high-efficiency bifunctional air electrocatalysts [12–14]. Therefore, the development of low-cost, highly efficient and excellent durability bifunctional electrocatalysts with high performance for both ORR and OER is critical toward the practical application of ZnABs.

Currently, transition metal and their derivations (oxides and hydroxide), as a new type of nonprecious electrocatalysts, have been developed and utilized as advanced electrode materials in various energy conversion and storage applications [15–19]. Especially, their nanostructures (such as nanosheets, nanoflakes, etc.) have attracted the attentions due to high electrocatalytic activity [20–24]. In particular, NiO, as one of the most famous metal oxides, has received considerable interest to the scientific and commercial fields owing to its enhanced safety, outstanding catalytic activity and the widespread availability [25–27]. Unfortunately, difficulties have been encountered in the NiO catalyst due to its rapid capacity and poor cycling durability, which is maybe derived from the phase transformation of α-Ni(OH)$_2$ into the thermodynamically stable β-Ni(OH)$_2$, decreasing the electrical conductivity, electrochemical performance, and reversibility [28,29].

---

* Corresponding authors.
  E-mail addresses: hongzhang@lzu.edu.cn (H. Zhang), gaodq@lzu.edu.cn (D. Gao).

Hence, a variety of strategies have been adopted to improve the electrical conductivity, increase active sites, and further enhance the electrochemical activity for ORR and OER of NiO by reducing their nanoscale. Doping has been proved as the effectively strategy to simultaneously increase the electrical conductivity, active sites and cycle stability [30,31]. In particular, it is demonstrated that the Co dopants could effectively improve the stability and conductivity of NiO, also has good activity toward hydrogen evolution reaction in alkaline solutions [32,33].

Hence, porous Co-NiO NFs as bifunctional catalysts for high-performance ZnABs is reported. Encouragingly, the as-obtained Co-NiO NFs yield remarkable electrocatalytic properties with the satisfactory half-wave potential of 0.79 V for ORR and low overpotential of 1.53 V at 10 mA cm^{-2} for OER. As a result, assembled ZnABs with Co-NiO NFs as air cathode exhibits a high discharge peak power density of 93 mW cm^{-2}, maximum specific capacity of 830 mA h g^{-1}, together with favourable stability without obvious decay after 110 h. More importantly, the corresponding all-solid state ZnABs demonstrate good performance with long-time cycling stability (6 h), and excellent flexible nature enough to the repeatedly bent. This finding makes Co-NiO NFs an outstanding bifunctional electrocatalysts in future energy storage devices.

2. Experimental

2.1. Synthesis of pristine and Co-NiO NFs

The Co-NiO NFs are composed of porous and regular hexagonal nanosheets, which were fabricated by a modified hydrothermal method [34]. Typically, 1.5 mmol Ni(NO$_3$)$_2$·6H$_2$O, 0.08 mmol Co(NO$_3$)$_2$·6H$_2$O, 3 mmol NH$_4$F and 7.5 mmol urea were dissolved in 70 ml of distilled water and constant stirring with a magnetic stirrer to form uniform green solution. After transferred into 100 ml Teflon-lined stainless autoclaves and sealed, it was maintained at 150 ℃ for 6 h and cooled down naturally to room temperature. Then the products were collected by washing three times with anhydrous ethanol and deionized water respectively, and dried thoroughly at 60 ℃. After that the calcination process was carried out at 300 ℃ in air for 2 h with a heating rate of 3 ℃ min^{-1}. The Co contents in the Co-NiO composite was calculated as about 4 at. % based on the Inductively Coupled Plasma Optical Emission Spectrometer (ICP-OES). Pristine NiO NFs were synthesized by using the similar method only without adding Co(NO$_3$)$_2$·6H$_2$O.

2.2. Material characterizations

X-ray diffraction (XRD) spectra were performed on a Philips/X, Pert Pro diffractometer with Cu $K\alpha$ radiation to analyze crystalline structure. Scanning electron microscope (SEM) and transmission electron microscope (TEM) characterizations were taken on a Hitachi S-4800 SEM and a Tecnai G2 F30, FEI to observe the morphologies and nanostructures of the samples. Raman spectra was collected on a Jobin-Yvon Labram HR80. X-ray photoelectron spectroscopy (XPS) spectra were carried out on a Kratos Axis Ultra to investigate the chemical states of the samples.

2.3. Electrochemical measurements

The electrochemical measurements were performed on a CHI 660E electrochemical workstation at room temperature with a typical three-electrode cell, including a glassy carbon working electrode coated with electrocatalysts, a Ag/AgCl reference electrode, and a platinum foil counter electrode. The linear sweep voltammetry curves were recorded at a scan rate of 2 mV s^{-1} in 0.1 M KOH and 1 M KOH as the electrolyte for all ORR and OER tests at room temperature, respectively. The measured potentials (vs Ag/AgCl) were converted to the RHE based on the Nernst equation (E$_{RHE}$＝E$_{Ag/AgCl}$＋0.197 + 0.059*pH). For accurate measurement in this work, 10 mg of the electrocatalyst and Nafion (30 μL, 5 wt. %) were added into 1470 μL N, N dimethylformamide,

which were sonicated for 5 h to form good electrochemical dispersion. Then the fresh ink catalyst (12.6 μL) was dropped onto rotating disk working electrode (RDE) with an electrocatalyst loading of 0.2 mg cm^{-2} and then dried at 60 ℃. The electrochemical impedance spectroscopy (EIS) measurements were performed over a frequency range 0.1-10^4 Hz. The turnover frequency (TOF) were calculated as mentioned in the previous report (Supporting Information) [35]. The number of electons transferred (n) was determined by using Koutecky-Levich equation as follow:

$$\frac{1}{j} = \frac{1}{j_k} + \frac{1}{j_l} = \frac{1}{j_k} + \frac{1}{B\omega^{1/2}} \tag{1}$$

$$B = 0.2nFC_0D_0^{2/3}\vartheta^{-1/6} \tag{2}$$

Where j and j_k are the measured and kinetic current densities, respectively, B is the Levitch constant. F is the Faraday constant, ω is the rotation speed (rpm). D_0 is the diffusion coefficient of oxygen in the electrolyte solution ($D_0 = 1.9*10^{-5}$). ϑ is the coefficient of motion viscous in the electrolyte solution (0.01 cm^2 s^{-1} for 0.1 M KOH), and C_0 is the bulk concentration of oxygen (1.2*10^{-6} mol cm^{-3}) [36,37].

2.4. ZnABs measurements

For liquid ZnABs, a two-electrode configuration in 6 M KOH or 6 M KOH with 0.2 M zinc acetate for primary and rechargeable ZnABs was employed, comprising a Zn foil as the counter electrode, the air electrode is a carbon fiber paper (CFP) loaded with above homogeneous electrocatalyst ink, with a mass loading of 2 mg cm^{-2}. Battery performance was taken on the potentiostat (CHI 760E, CH Instrument Co.) and LAND testing system.

2.5. Button-like all-solid-state ZnABs

A photograph of the arrangement of the relevant components in the button battery is shown in Supporting Information (Fig. S2), it can be seen that the button cell was assembled with Co-NiO NFs dropped CFP as the air cathode, a polished Zn plate was used as anode, polyvinyl alcohol (PVA) glue as electrolyte. The Zn foil with adequate PVA glue (Zn/PVA) was first assembled, then the Co-NiO NFs loaded CFP was tightly embraced the newly assembled Zn/PVA with a parafilm, this simple solid-like ZnABs was assembled to further verify the flexible nature by bending different angles. The PVA glue was prepared as follow: 2 g PVA powder was dissolved in 20 ml deionized water at 95 ℃ under continue magnetic stirring for 2 h until a transparent gel was formed, then 2 ml 18 M KOH was added into the solution and stirred for 40 min to form a homogeneous solution. Finally the solution was frozen into solid and then thawed.

2.6. Calculation details

The generalized gradient approximation (GGA) was employed to calculate the band structure and the density of states (DOS) for NiO with and without Co doping as previously reported (Supporting Information) [38,39].

3. Results and discussion

The Co-NiO NFs were synthesized by a simple hydrothermal method, which displays uniform flower-like shape with the sound 2D hexagonal framework and numerous nanopores inside the nanosheets. X-ray diffraction (XRD) studies of pristine NiO and Co- NiO NFs shown in Fig. 1a, indicating that all diffraction peaks are in good agreement with NiO (JCPDS # 02-1216), confirming the high purity of the as-synthesized samples. No second phase or precipitation were generated in the formation of Co-NiO NFs, verifying that the Co were successfully incorporated into the NiO matrix. And the enlarged view of the XRD
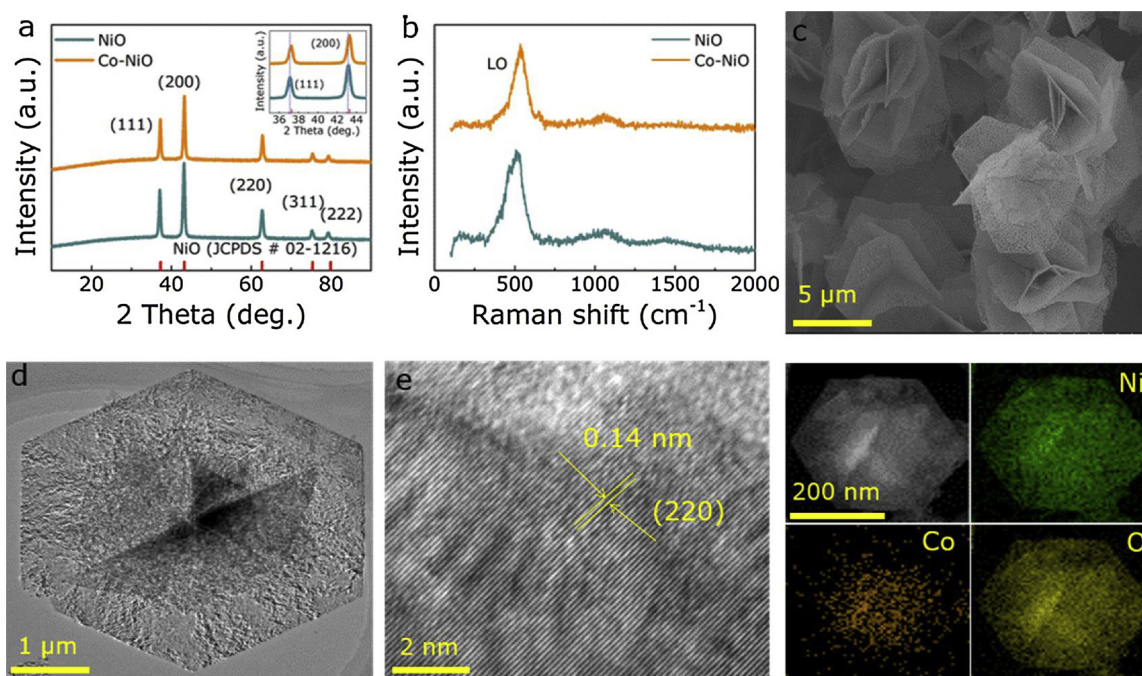
Fig. 1. The detailed structure and morphology of Co-NiO and pristine NiO NFs. (a) XRD patterns and (b) Raman spectra of Co-NiO and pristine NiO NFs. The inset in (a) presents an enlarged view of XRD pattern. (c) SEM images of Co-NiO NFs. (d) TEM and (e) HRTEM images of Co-NiO NFs. (f) Element mappings of Co-NiO NFs.

pattern is displayed in the inset of Fig. 1a, which shows a slight shift to higher angles due to the smaller ionic radius of Co^{2+} (0.65 Å) than Ni^{2+} (0.69 Å), indicating the substitution of Co^{2+} for Ni^{2+} [40,41]. Raman spectra further confirms the phase structure of NiO. As shown in Fig. 1b, the peak located at $550\,cm^{-1}$ can well assigned as the first-order longitudinal optical (LO) phonon modes of cubic NiO. It is obvious that the Raman spectra of Co-NiO NFs show similar characteristics to pure NiO, demonstrating that the crystal feature of NiO is not changed after Co doping [42]. Further, the morphology and structures of the Co-NiO and NiO NFs were examined by SEM and TEM. As presented in Fig. 1c–d, uniform ultrathin porous flower-like Co-NiO composed of the regular hexagonal nanosheets, which can significantly facilitate the adsorption and diffusion of O_2 during OER and ORR [43–45]. In addition, a typical high-resolution TEM image (Fig. 1e) displays lattice spacing with spacing of 0.14 nm that is indexed to the (220) planes of the cubic NiO phase, confirming the well-crystalline structure of the sample. It can be assumed that this ultrathin 2D, flower-like structure with numerous nanopores inside the nanosheets can provide an ideal catalyst platform for exploring and utilizing more catalytic active sites, further improving its electrochemical performance. STEM-EDS analysis (Fig. S3, Supporting Information) and EDX elemental mapping were performed to analyze the spatial elemental existence and distribution. As shown in Fig. 1f, Ni, Co and O elements are uniformly distributed in Co-NiO matrix, corroborating the successful doping of Co into NiO.

The surface compositions and chemical states of both samples were further detected by XPS (Fig. 2 and Fig. S4 (Supporting Information)).The full survey spectrum is shown in Fig. S4a (Supporting Information), from which the presence of C, Ni, Co, and O without other impurities are indicated. As illustrated in Fig. 2a, the Co 2p high-resolution spectrum of Co-NiO NFs is fitted with three spin-orbit doublets, the peaks located at 779.8 eV and 795.4 eV are corresponding to Co^{2+}, and the peaks at 782.0 eV and 796.4 eV are consistent of Co^{3+}, other peaks located at 784.9 eV and 798.9 eV are assigned to satellite structure [46–48]. Fig. 2b shows the high-resolution Ni 2p spectrum of Co-NiO NFs which can be also fitted into three spin-orbit doublets, the peaks at 853.8 eV and 871.3 eV are assigned with Ni^{2+}, and the peaks located at 855.7 eV and 872.7 eV are attributed to Ni^{3+}, other peaks at

861.1 eV and 878.7 eV are corresponding to satellites [49,50]. Fig. 2c displays the high-resolution O 1s spectrum, where the peaks at 530.6 eV and 529.2 eV are assigned to the oxygen species [51,52]. The high-resolution Ni 2p and O 1s of pristine NiO NFs are shown in Fig. S4b–c (Supporting Information), and the XPS fitting results are displayed in Tables 1–3 (Supporting Information). Hence, above analyzed physical characterizations (XPS compared with XRD, SEM and TEM) amply verify the successful production of Co-NiO NFs bifunctional catalysts. The DOS diagrams of pristine and Co-NiO are displayed in Fig. 2d and e, respectively. It can be seen that Co-NiO reveals a metallic-like nature with a greater electron occupied state at the Fermi level compared with the pristine NiO with the band gap 3.1 eV, corroborating that it is possible to increase the charge transfer during OER and ORR process for Co-NiO. In addition, Fig. 2f shows the partial charge density of the Co-NiO to visualize the distribution of conducting charges uniformly spread, which can efficiently accelerate charge transfer over the catalytic electrode and further promote the electrocatalytic activity of NiO.

The electrochemical ORR activities of pristine NiO and Co-NiO NFs was evaluated in the electrode of 0.1 M KOH with a slow scan rate of $2\,mV\,s^{-1}$. As shown in Fig. 3a, Co-NiO NFs exhibits the good ORR performance with an onset potential of 0.92 V and a half-wave potential of 0.79 V (vs. RHE), which are more positive than pristine NiO NFs (the onset potential is 0.89 V and the half-wave potential is 0.76 V), although which is lower than commercial Pt/C (the onset potential is 0.96 V and the half-wave potential is 0.81 V). Meanwhile, the Co-NiO NFs shows the smaller Tafel slope of $133\,mV\,dec^{-1}$ (Fig. S5, Supporting Information) comparable to the pristine NiO NFs ($153\,mV\,dec^{-1}$), demonstrating a highly pronounced facilitated O_2 diffusion in the air electrode based on Co-NiO NFs catalyst [53]. The linear sweep voltammetry (LSV) curves of ORR for Co-NiO NFs catalyst at various rotating speeds are shown in Fig. 3b to further gain insight to the ORR kinesics, where the current density shows an increasing tend with rotating speed increases, affirming a first-order reaction toward oxygen reduction [54,55]. The average number of electrons transferred per oxygen molecule (*n*) is calculated to be the 3.49 at various potentials for Co-NiO NFs (inset in Fig. 2b), indicating a close four-electron transfer process can reduce oxygen effectively than a two-electron pathway of pristine NiO NFs catalyst [56]. (Fig. S6a, Supporting Information.) To
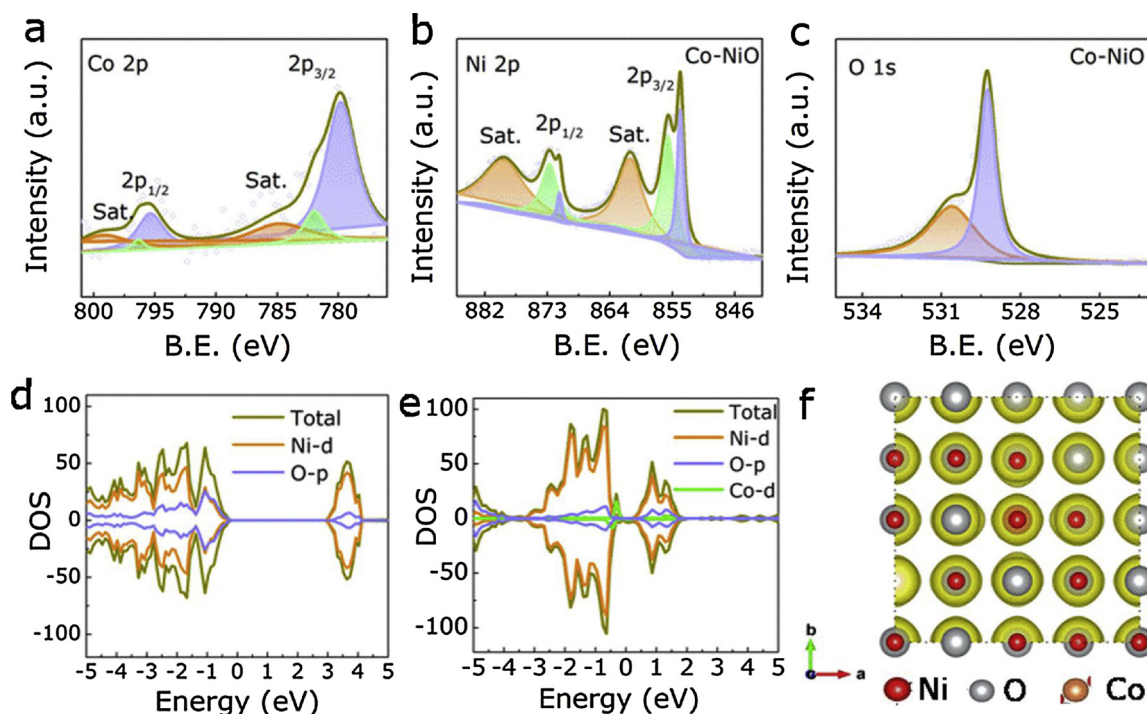
Fig. 2. XPS spectra of Co-NiO NFs. (a) Co 2p (b) Ni 2p. (c) O 1s. The DOS diagrams of pristine NiO (d) and Co-NiO (e). (f) The partial charge density of the Co-NiO.

further corroborate the good ORR catalytic activity of Co-NiO NFs, rotating ring-disk electrode (RRDE) voltammograms were measured at 1600 rpm, where the disk currents reflect ORR electrocatalysis and the ring currents are associated with the oxidation of generated intermediate peroxide species (Fig. 3c). For Co-NiO NFs catalyst, the calculated n is about 3.6 and peroxide percentage is about 15% over the potential range of 0.2-0.7 based on the RRDE data, much better than the pristine NiO NFs as illustrated in Fig. S6a–b (Supporting

Information), suggesting the Co-NiO NFs catalyze the ORR via an apparent four-electron pathway similar to Pt/C [57]. This result in accordance with the conclusion from the Koutecky-Levich (K–L) curves constructed at different rotation rates. Therefore, higher n and lower peroxide yield again verity the increased ORR kinetic properties owing to the Co doping.

Furthermore, in the context of developing ORR-OER bifunctional catalysts, exploring the activity towards catalyzing OER of Co-doped
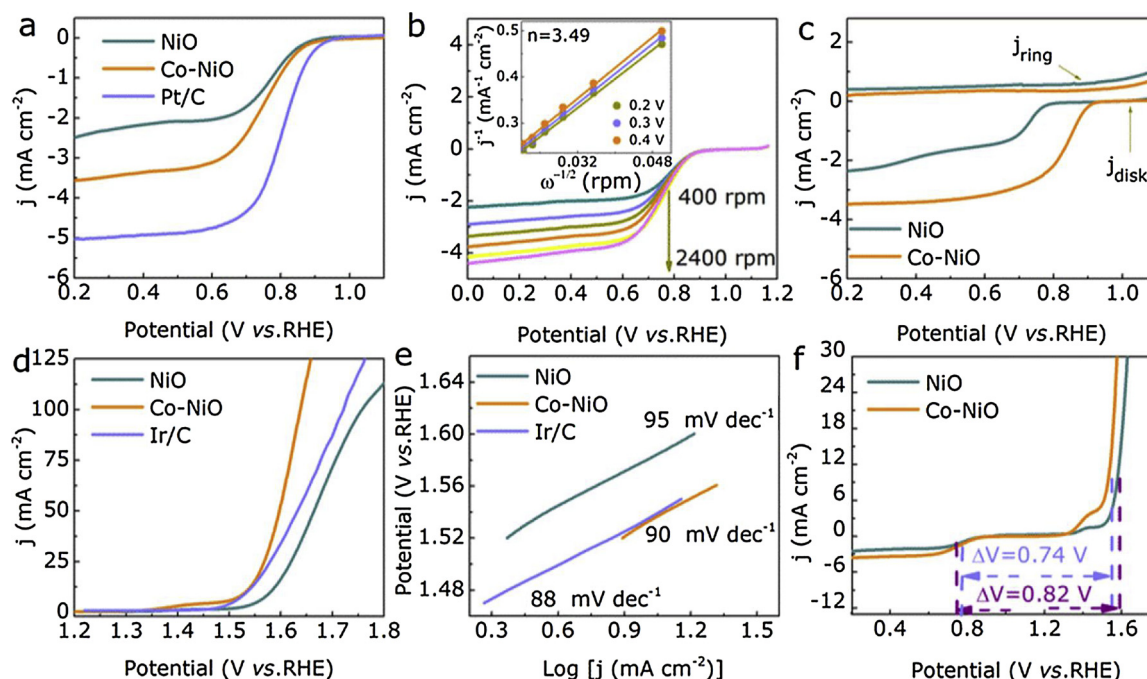

Fig. 3. Electrochemical activities of Co-NiO and pristine NiO NFs catalysts. (a) LSV curves of ORR at 1600 rmp of all the catalysts and (b) LSV curves of ORR at different rotating speeds of Co-NiO NFs. The inset of (b) is K–L plots of Co-NiO NFs at different potentials. (c) Linear voltammograms of Co-NiO NFs measured using RRDEs. (d) LSV curves of OER for all the catalysts. (e) Tafel plots obtained from the corresponding LSV curves for all the catalysts. (f) ORR and OER curves of Co-NiO and pristine NiO NFs catalysts.
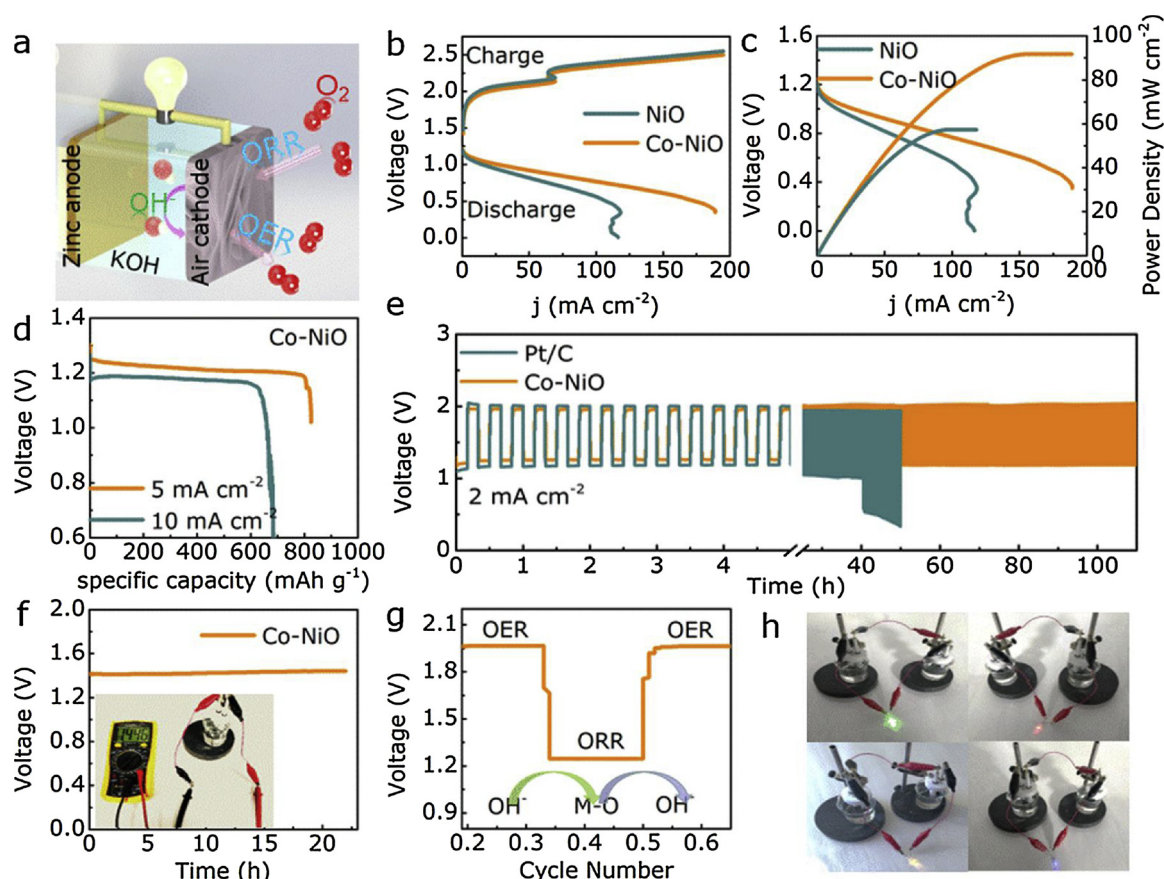
Fig. 4. Electrochemical performance of the ZnABs with the Co-NiO and NiO NFs electrode. (a) A schematic configuration of ZnABs. (b) Charge and discharge polarization curves of Co-NiO NFs based ZnABs. (c) Polarization and power density curves of the primary ZnABs. (d) Specific capacities of the primary ZnABs normalized to the mass of the consumed Zn at the current density of 5 and 10 mA cm^{-2}, respectively. (e) Galvanostatic discharge–charge cycling curves at 2 mA cm^{-2} of rechargeable ZnABs. (f) Open curve and photograph (inset) of ZnABs with the Co-NiO NFs electrode. (g) Charge-discharge-charge voltage profiles at current densities of 2 mA cm^{-2}. (h) Photogtaph of green, red, yellow, and blue LEDs powered by two ZnABs with the Co-NiO NFs air cathode connected in series. (For interpretation of the references to colour in this figure legend, the reader is referred to the web version of this article.)

NFs, is of paramount importance. So the electrocatalytic OER performance of Co-NiO NFs, pristine NiO NFs were studied first using linear scan voltammogram (LSV). As shown in Fig. 3d, the Co-NiO NFs exhibits the good OER performance with a significantly low potential of 1.53 V (vs. RHE) at 10 mA cm^{-2}, which is lower than that of pristine NiO NFs (1.58 V). To gain further insight into these catalysts, the Tafel plots are calculated to investigate the OER kinetic process of as-synthesized electrocatalysts [58]. As shown in Fig. 3e, the Tafel slope of Co-NiO NFs is 90 mV dec^{-1}, which is superior to the pristine NiO NFs (95 mV dec^{-1}), suggesting its faster OER kinetics. In addition, the double layer capacitance (C_{dl}) was further measured to evaluate the effective electrochemical active surface area (ECSA) of as-synthesized electrocatalysts, because C_{dl} is proportional to ECSA [58,59]. The C_{dl} of Co-NiO NFs is 28.5 mF cm^{-2}, corresponding to the largest ECSA (237.5 m^2 g^{-1}), higher than that of pristine NiO NFs with the C_{dl} of 18.5 mF cm^{-2} (Fig. S7b, Table S4, Supporting Information), evidencing Co-NiO NFs can provide more active sites for redox reaction. Furthermore, electrochemical impedance spectroscopy (EIS) was measured to assess the impedance properties of samples, as shown in Fig. S6c (Supporting Information), Co-NiO NFs catalyst reveals a lower charge transfer resistance (R_{ct}) of 58 ohm than that of pristine NiO NFs catalyst (80 ohm), as indicated from the smaller size of the semicircle in the high frequency range (Fig. S7c, Supporting Information), further demonstrating its higher conductivity and faster OER kinetic properties [58,60,61]. The turnover frequencies (TOF) was also employed to investigate the catalytic kinetic towards the OER, as shown in Fig. S7d (Supporting Information), the TOF value of Co-NiO NFs (4.4 O$_2$ s^{-1} at

the potential at 1.5 V) is superior than that of the pristine NiO NFs (3.2 O$_2$ s^{-1}), further revealing the significance of Co-NiO NFs electrocatalyst for the OER [62–64]. Besides, Fig. S7e (Supporting Information) displays no change on the LSV of Co-NiO NFs before and after 10,000 CV cycles, revealing that the Co-NiO NFs catalyst exhibits good stability for OER. Chronoamperometry test also attested stability of Co-NiO NFs catalyst with only 3% reduction in the current density of its initial activity after about 20 h operation at a constant potential of 1.45 V (Fig. S7f, Supporting Information). Furthermore, no obvious changes on phase structure, binding energies and morphology are observed after OER test, confirming the good OER structure stability of Co-NiO NFs (XRD, XPS, TEM results, shown in Fig. S8, Supporting Information). Besides, the influence of Co doping amount on electrochemical ORR/OER activity of Co-NiO NFs was also discussed, as shown in Table S5 and Fig. S9 (Supporting Information), with the increase of Co doping amount, the electrocatalytic OER/ORR performance shows a trend of increasing first and then decreasing. Co-NiO NFs shows the optimal catalytic activity when the Co doping amount is 4 at. %, indicating overdoping will inhibit the ORR/OER performance of Co-NiO NFs.

The overall oxygen activity of the Co-NiO NFs as bifunctional catalysts can be evaluated by the potential difference (ΔE) between the $E_{j=10}$ for OER and $E_{1/2}$ for ORR (ΔE = $E_{j=10}$ - $E_{1/2}$), with the smaller ΔE for the better reversible oxygen electrode [65,66]. Obviously, the Co-NiO NFs catalyst displays a low ΔE of 0.74 V as shown in Fig. 3f, which is much lower than that of pure NiO NFs and most NiO-based electrocatalysts (Table S6, Supporting Information). The superior bifunctional OER/ORR catalytic activity and reversibility based on Co-NiO NFs are
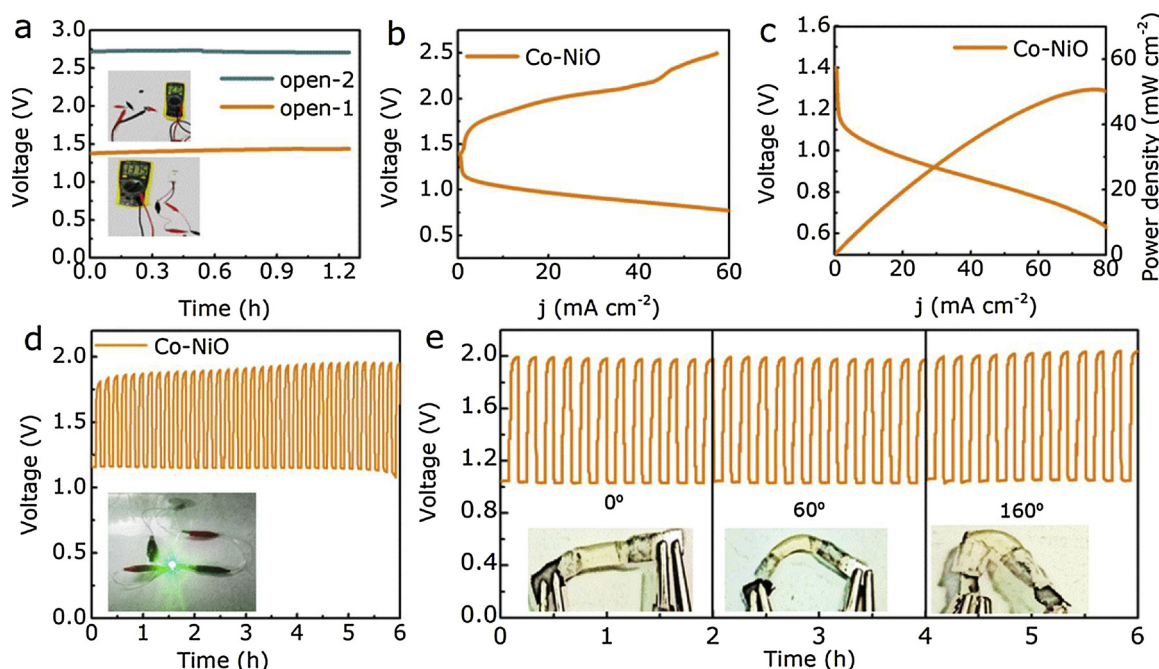
Fig. 5. Electrochemical performance of the all-solid-state ZnABs with the Co-NiO NFs electrode. (a) Open curve and photograph (inset) of one (blue curve) and two button-like all-solid-state ZnABs in series (orange curve). (b) Charge and discharge polarization curves and (c) polarization and power density curves of the button-like all-solid-state ZnABs. (d) Galvanostatic discharge–charge cycling curves at 2 mA cm^{-2} of all-solid-state ZnABs (Inset: Photogtaph of a green LED powered by one button-like all-solid-state ZnABs with the Co-NiO NFs air cathode and (e) bending to 0°, 60°, and 160° every 2 h. (For interpretation of the references to colour in this figure legend, the reader is referred to the web version of this article.)

likely to contributed to three major factors. First, the atomic Co doping enhances the intrinsic activity per active site and simultaneously increases the conductivity of pure NiO NFs, as is confirmed by the calculation, LSV, EIS results. Second, the large effective electrochemical active surface area of Co-NiO NFs is beneficial to exposing and utilizing more electroactive sites, which can effectively facilitate the OER/ORR activity, as is confirmed by the calculated C_{dl} values. Third, the synergistic effect between the sound 2D hexagonal framework and numerous nanopores structure can provide an ideal surfaces for oxygen absorption and diffusion, as is confirmed by the Tafel slope. On the whole, the successful engineering of structure of Co-NiO NFs with numerous nanopores inside the nanosheets has synergistically realized sufficient gas transport, abundant catalysts active sites, and satisfactory intrinsic activity. These results also provide reliable condition for further investigating its feasibility in realistic primary and rechargeable ZnABs based on the Co-NiO NFs catalyst.

Hence, on the basis of the bifunctional activity discussed above for Co-NiO NFs, primary ZnABs were constructed using Co-NiO NFs loaded onto a carbon fiber paper (CFP) substrate as the air electrode (also using pure NiO NFs for comparison), a Zn foil as the anode, and 6.0 M KOH with 0.2 M Zinc acetate as the electrolyte (Fig. 4a). Fig. 4b shows the cathodic and anodic polarization curves of Co-NiO and pure NiO NFs based ZnABs, and a small charge-discharge voltage gap of 1.17 V at current density of 50 mA cm^{-2} for Co-NiO NFs based ZnABs, which is lower than that of pristine NiO NFs (1.30 V). As illustrated in Fig. 4c, the peak power density reaches to 93 mW cm^{-2} at 0.6 V for Co-NiO NFs based ZnABs, which is significantly greater than the peak power density of pure NiO NFs based ZnABs (57 mW cm^{-2}). In addition, the Co-NiO NFs based ZnABs exhibit long-time durability, which can stable up to 20 h when discharged at 5 mA cm^{-2} (Fig. S10, Supporting Information). Further, the specific discharge capacity was found to be 830 mA h g^{-1} at 5 mA cm^{-2} for Co-NiO NFs based ZnABs (normalization by the mass of the consumed Zn in the Zn anode), corresponding to a high energy density of 962 Wh kg^{-1}, which is superior to the pure NiO NFs based ZnABs. When increasing the current density to 10 mA cm^{-2}, the

specific capacity reaches to about 700 mA h g^{-1} (Fig. 4d). A long-time charge-discharge cycle test was performed with a current density of 2 mA cm^{-2} (Fig. 4f and Fig. S11 (Supporting Information)), the Co-NiO NFs shows an initial charge of 1.97 V and discharge potential of 1.25 V with a voltage gap of 0.72 V and a round-trip efficiency of 63%. After continuous 110 h operation, the voltage gap only slightly increased about 100 mV and the round-trip maintained at 58%. These results further demonstrate the superior durability and the good cycle performance for Co-NiO NFs based ZnABs, which is obviously better than pure NiO NFs and Pt/C based ZnABs. In addition, Fig. 4g further detailed indicates the initial charge-discharge cycle process. In the first charge stage, the flat voltage plateau at 1.25 V illustrated the OER process, while the voltage regions corresponded to the ORR afterward in the discharge stage, demonstrating again that Co-NiO NFs is the high performing bifunctional catalyst during the discharging and charging processes. The light-emitting diodes (LED) with different colours could be powered by two ZnABs in series with the Co-NiO NFs as air cathode (Fig. 4h), further underscoring the potential for applying Co-NiO NFs based ZnABs to portable devices. Further, button-like all-solid-state ZnABs were assembled using Co-NiO NFs coated onto CFP substrate as the air electrode. (Fig. S2, Supporting Information). As shown in Fig. 5a, this button cell remains a steady open-circuit voltage of 1.38 V and a high sufficiently high open-circuit voltage of 2.75 V for two ZnABs in series, capable of powering a green LED (inset in Fig. 5d). As displayed in Fig. 5c, the Co-NiO NFs based button cells shows a 1.02 V voltage difference between charge and discharge process at 20 mA cm^{-2}, and the peak power density reached 50 mW cm^{-2} at 0.67 V (Fig. 5d). Furthermore, this button cells show superior durability with a considerably stable charge voltage of 1.87 V and a discharge voltage of 1.16 V with virtually negligible voltage fading for 6 h as shown in Fig. 5d. Besides, the flexible nature of the solid-like ZnABs was evaluated by the cycling stability at different bending angles (0°, 60°, 160°) for every 2 h, where the charge-discharge voltage basically stable, demonstrating the potential for applying Co-doped NFs to flexible electronics (Fig. 5e). Thus, the Co-NiO NFs are the more promising

bifunctional catalyst for further developing ZnABs with excellent power density while maintaining high energy density and long-time durability.

4. Conclusions

In summary, Co-NiO NFs with the sound 2D hexagonal framework and numerous nanopores inside the nanosheets have been obtained by a simple hydrothermal method. The resultant Co-NiO NFs demonstrates prominent bifunctional electrocatalytic activity toward both ORR and OER, superior to the pristine NiO electrocatalyst, even outperformed commercial Ir/C electrocatalyst for OER. The observed excellent electrocatalytic activities can be attributed to the unique flower-like structure of Co-NiO NFs with porous inside the nanosheets, which provides an adequate surface for O_2 adsorption/diffusion, and a large effective electrochemical active surface area. Furthermore, Co doping effectively increases the conductivity of pristine NiO NFs and significantly enhances the intrinsic activity of ORR and OER. Besides, the liquid ZnABs with engineered Co-NiO NFs electrode shows a high discharge peak power density of 93 mW cm^{-2} and excellent device stability (no obvious weaken after 110 h). Additionally, all-solid-state ZnABs assembled with Co-NiO NFs demonstrates the superior durability (more than 6 h of charge and discharge cycles) and good flexible nature (no obvious voltage change when bent to various angles). These promising results provide a new strategy for exploring non-precious metal-based bifunctional electrocatalysts for superior power/energy density and durability ZnABs.

Conflicts of interest

There are no conflicts of interest to declare.

Acknowledgements

Appendix A. Supplementary data

Supplementary material related to this article can be found, in the online version, at doi:https://doi.org/10.1016/j.apcatb.2019.03.021.

References

[1] G.T. Fu, Y. Liu, Y.F. Chen, Y.W. Tang, J.B. Goodenough, J.M. Lee, Nanoscale 10 (2018) 19937–19944.
[2] K.M. Naik, S. Sampath, Electrochim. Acta 292 (2018) 268–275.
[3] J.T. Ren, G.G. Yuan, C.C. Weng, L. Chen, Z.Y. Yuan, Chemcatchem 10 (2018) 5297–5305.
[4] Yanguang Li, Hongjie Dai, Chem. Soc. Rev. 43 (2014) 5257–5275.
[5] B. Hua, M. Li, W. Pang, W. Tang, S. Zhao, Z. Jin, Y. Zeng, B. Shalchi Amirkhiz, J.L. Luo, Chemistry 4 (2018) 2902–2916.
[6] D.S. Geng, N.N. Ding, T.S.A. Hor, S.W. Chien, Z.L. Liu, Y. Zong, RSC Adv. 5 (2015) 7280–7284.
[7] M. Wu, Y. Wang, Z. Wei, W. Lei, Z. Ming, J. Zhang, X. Han, J. Ma, J. Mater. Chem. A (2018) 10.1039.C1038TA02416B.
[8] X. Liu, H. Li, W. Wan, H. Liu, S. Shen, L. Fang, J. Luo, Chemelectrochem 5 (2018) 1113–1119.
[9] S.J. Gerssen-Gondelach, A.P.C. Faaij, J. power sources 212 (2012) 111-129.
[10] T. Li, Y. Lu, S. Zhao, Z. Gao, Y.Y. Song, J. Mater. Chem. A 6 (8) (2018) 3730–3737.
[11] W. Wenjun, L. Xijun, L. Huaiyu, P. Xianyun, X. Desheng, L. Jun, Appl. Catal. B 240 (2019) 193–200.
[12] Y.H. Qian, Z.G. Hu, X.M. Ge, S.L. Yang, Y.W. Peng, Z.X. Kang, Z.L. Liu, J.Y. Lee, D. Zhao, Carbon 111 (2017) 641–650.
[13] C. Hu, L. Dai, Angew. Chem. Int. Ed. Engl. 55 (2016) 11736–11758.
[14] L. Xin, F. Yang, S. Rasouli, Y. Qiu, Z.F. Li, A. Uzunoglu, C.J. Sun, Y. Liu, P. Ferreira, W. Li, ACS Catal. 6 (2016) 2642–2653.
[15] B.F. Cao, G.M. Veith, J.C. Neuefeind, R.R. Adzic, P.G. Khalifah, Cheminform 45 (2014) 19186.
[16] Y. Zhao, R. Nakamura, K. Kamiya, S. Nakanishi, K. Hashimoto, Nat. Commun. 4 (2013) 2390.
[17] G. Zhang, G. Wang, Y. Liu, H. Liu, J. Qu, J. Li, J. Am. Chem. Soc. 138 (2016) 14686.
[18] B. Hua, M. Li, Y.F. Sun, Y.Q. Zhang, N. Yan, J. Chen, T. Thundat, J. Li, J.L. Luo, Nano Energy 32 (2017) 247–254.
[19] C. Lin, L. Qu, J. Li, Z. Cai, H. Liu, P. He, X. Xu, L. Mai, Nano Res. (2019) 205–210.
[20] L. Ji, F.Z. Rui, M.C. Xue, Adv. Mater. 26 (2014) 6074–6079.
[21] Y. Li, M. Gong, Y. Liang, J. Feng, J.E. Kim, H. Wang, G. Hong, B. Zhang, H. Dai, Nat. Commun. 4 (2013) 1805.
[22] U.L. Dong, J.Y. Choi, K. Feng, H.W. Park, Z. Chen, Adv. Energy Mater. 4 (2014).
[23] P. Da, M. Wu, K. Qiu, D. Yan, Y. Li, M. Jing, C. Dong, L. Tao, S. Qiao, Chem. Eng. Sci. 194 (2019) 127–133.
[24] C. Xu, B. Liu, Z. Cheng, L. Zhi, L. Jie, M. Lu, Y. Deng, X. Han, T. Wu, W. Hu, Adv. Energy Mater. 7 (2017).
[25] D. Su, M. Ford, G. Wang, Sci. Rep. 2 (2012) 924.
[26] B. Zhao, X.K. Ke, J.H. Bao, C.L. Wang, L. Dong, Y.W. Chen, H.L. Chen, J. Phys. Chem. C 113 (2010) 14440–14447.
[27] B. Varghese, M.V. Reddy, Y. Zhu, S.L. Chang, T.C. Hoong, G.V.S. Rao, B.V.R. Chowdari, A.T.S. Wee, C.T. Lim, C.H. Sow, Chem. Mater. 20 (2008) 3360–3367.
[28] A.L. Brisse, P. Stevens, G. Toussaint, O. Crosnier, T. Brousse, Materials 11 (2018).
[29] B.K. Kim, V. Chabot, A. Yu, Electrochim. Acta 109 (2013) 370–380.
[30] M.H. Ryu, K.N. Jung, K.H. Shin, K.S. Han, S. Yoon, J. Phys. Chem. C 117 (2013) 8092–8098.
[31] Q. Wang, Y. Huang, J. Miao, Y. Zhao, W. Zhang, Y. Wang, J. Am. Ceram. Soc. 96 (2013) 2190–2196.
[32] Z. Zheng, L. Huang, Y. Zhou, X. Hu, X. Ni, Solid State Sci. 11 (2009) 1439–1443.
[33] P. Tan, B. Chen, H.R. Xu, W.Z. Cai, W. He, M. Ni, Electrochim. Acta 290 (2018) 21–29.
[34] Y.J. Mai, J.P. Tu, X.H. Xia, C.D. Gu, X.L. Wang, J. Power Sources 196 (2011) 6388–6393.
[35] P. Liu, D. Gao, W. Xiao, L. Ma, K. Sun, P. Xi, D. Xue, J. Wang, Adv. Funct. Mater. 28 (2018) 1706928.
[36] I.S. Amiinu, Z. Pu, X. Liu, K.A. Owusu, H.G.R. Monestel, F.O. Boakye, H. Zhang, S. Mu, Adv. Funct. Mater. 27 (2017) 1702300.
[37] B.Y. Xia, H.B. Wu, N. Li, Y. Yan, X.W. Lou, X. Wang, Angew. Chem. 54 (2015) 3797–3801.
[38] A. Rohrbach, J. Hafner, G. Kresse, Phys. Rev. B 69 (2004) 428–433.
[39] S. Park, H.S. Ahn, C.K. Lee, H. Kim, H. Jin, H.S. Lee, S. Seo, J. Yu, S. Han, Phys. Rev. B Condens. Matter 77 (2008).
[40] A.K. Mishra, D. Das, Pts A and B 1349 (2011) 1139–1140.
[41] X. Hui, Z. Min, L. Jing, X. Tong, RSC Adv. 5 (2015) 91493–91499.
[42] N. Mironova-Ulmane, A. Kuzmin, I. Steins, J. Grabis, I. Sildos, M. Pars, J. Phys. Conf. Ser. 93 (2007).
[43] Y. Xue, M. He, S. Sun, W. Qin, S. Li, Z. Liu, J. Power Sources 297 (2015) 202–207.
[44] J. Pan, Y.Y. Xu, H. Yang, Z. Dong, H. Liu, B.Y. Xia, Adv. Sci. 5 (2018) 1700691.
[45] Z. Zhu, J. Ping, X. Huang, J. Hu, Q. Chen, X. Ji, J. Mater. Sci. 47 (2012) 503–507.
[46] J. Zhang, G. Cai, Z. Ding, T. Hong, X. Wang, C. Gu, J. Tu, J. Mater. Chem. C Mater. Opt. Electron. Devices 2 (2014) 7013–7021.
[47] A. Tiwari, A. Gupta, Appl. Phys. Lett. 88 (2006) 160.
[48] L. Yan, J.S. Pan, C.K. Ong, Mater. Sci. Eng. B 128 (2006) 34–36.
[49] M.A. Peck, M.A. Langell, Chem. Mater. 24 (2012) 4483–4490.
[50] S. Uhlenbrock, C. Scharfschwerdt, M. Neumann, G. Illing, H.J. Freund, J. Phys. Condens. Matter 4 (1992) 7973.
[51] T.V. Thi, A.K. Rai, J. Gim, J. Kim, J. Power Sources 292 (2015) 23–30.
[52] Vanchiappan Aravindan, P.S. Kumar, Jayaraman Sundaramurthy, W.Chui Ling, Seeram Ramakrishna, Madhavi, J. Power Sources 227 (2013) 284–290.
[53] L. Ji, D. Xin, C. Gibson, W.D. Xi, Z.Q. Shi, Adv. Mater. 25 (2013) 6226–6231.
[54] S. Zhao, W. Yun, J. Dong, C.T. He, H. Yin, P. An, K. Zhao, X. Zhang, G. Chao, L. Zhang, Nat. Energy 12 (2016) 16184.
[55] J. Feng, Y. Liang, H. Wang, Y. Li, B. Zhang, J. Zhou, J. Wang, T. Regier, H. Dai, Nano Res. 5 (2012) 718–725.
[56] J. Qiao, L.I. Xu, D. Lei, Z. Lei, Ryan BAKER, X. Dai, J. Zhang, Appl. Catal. B 125 (2012) 197–205.
[57] W. Wang, Y.C. Liu, J. Li, J. Luo, L. Fu, S.L. Chen, J. Mater. Chem. A 6 (2018) 14299–14306.
[58] D. Voiry, M. Chhowalla, Y. Gogotsi, N.A. Kotov, Y. Li, R.M. Penner, R.E. Schaak, P.S. Weiss, ACS Nano 12 (2018) 9635–9638.
[59] S. Trasatti, O.A. Petrii, Pure Appl. Chem. 63 (1991) 711–734.
[60] Z.Y. Shao, H. Qi, X. Wang, J. Sun, N.K. Guo, K. Huang, Q. Wang, Electrochim. Acta 296 (2019) 259–267.
[61] J. Dong, F.Q. Zhang, Y. Yang, Y.B. Zhang, H. He, X. Huang, X. Fan, X.M. Zhang, Appl. Catal. B 243 (2019) 693–702.
[62] D.N. Ding, K. Shen, X.D. Chen, H.R. Chen, J.Y. Chen, T. Fan, R.F. Wu, Y.W. Li, ACS Catal. 8 (2018) 7879–7888.
[63] X. Han, X. Wu, Z. Cheng, Y. Deng, N. Zhao, W. Hu, Nano Energy 31 (2017) 541–550.
[64] E. Fabbri, A. Habereder, K. Waltar, R. Kötz, T.J. Schmidt, Catal. Sci. Technol. 4 (2014) 3800–3821.
[65] C. Hu, L. Dai, Adv. Mater. 29 (2017).
[66] J. Zheng, K. Zhang, Y. Fang, Y. Zuo, Y. Duan, Z. Zhuo, X. Chen, W. Yang, Y. Lin, M.S. Wong, ACS Appl. Mater. Interfaces 7 (2015) 66.